UNDERSTANDING THE SELF-RECONFIGURATION PROPERTIES OF A NOVEL SPINEL-TYPE HIGH-ENTROPY CATALYST

Chunqun Qin[a], Chao Wang[a,*], Mingzheng Liao[a], Yanping Du[b,c**] Jiming Gao[d], Yanbing Wu[d]

[a] Guangdong Provincial Key Laboratory on Functional Soft Condensed Matter, School of Materials and Energy, Guangdong University of Technology, Guangzhou 510006, China

[b] School of Engineering, Lancaster University, Penryn Campus, Penryn, Cornwall TR109FE, UK

[c] China-UK Low Carbon College, Shanghai Jiao Tong University, Shanghai, 201306, China

[d] Guangdong Nengchuang Technology Co., Ltd, Guangzhou, 510000, China

Abstract: High-entropy oxides (HEOs), known for their excellent thermodynamic stability due to their high-entropy effect. In this study, high-entropy $(Ni_xAlCoCrMn)_3O_4$ oxides of spinel structure were synthesized by sol-gel method. This HEO has a self-reconfiguration properties in the reaction, and its internal Ni and Co ions exsolve to form a uniformly dispersed NiCo alloy on the surface. The increase of Ni content promotes the exsolution of Ni and Co ions from the interior of the spinel. The high-entropy with a large number of oxygen vacancies not only possesses a stable structure to limit the migration of NiCo alloys, but also enhances the hydrogen overflow. In the CO methanation reaction, it has 99% CO conversion with 87% methane selectivity within 400 ºC, and it is stable in the long-term test. This work provides a new idea for exploring the use of high-entropy materials to improve thermal catalytic activity and stability.

Key words: CO methanation，high-entropy oxides，self-reconfiguration

1. Introduction

As the energy industry shifts towards renewable and low-carbon technologies to combat climate change and resource depletion. Natural gas is widely used due to its relative cleanliness and high combustion efficiency [1, 2]. The artificial production of natural gas is considered a viable strategy to achieve this goal by converting syngas (a mixture of CO and H_2) derived from coal or biomass gasification through catalytic CO methanation [3]. The resulting methane, also known as substitute natural gas (SNG), can be directly integrated into the existing natural gas network [4, 5]. The SNG process mainly involves the gasification of raw materials (coal, biomass, industrial wastes, etc.), a syngas conversion reaction to adjust the hydrogen-to-carbon ratio ($H_2/CO > 3.0$), syngas purification (desulfurization and decarbonization), and methanation [6].

As shown in equation (1), the methanation of CO is thermodynamically favorable at low temperatures but is limited by chemical kinetics. However, low temperatures would trigger the carbon polarization reaction in CO shown in equation (2), leading to carbon deposition and destroying the physical structure of the catalyst surface [7, 8]. Among many metal catalysts, nickel (Ni), cobalt (Co), and other metals with strong adsorption capacities for CO and H_2 molecules have been widely employed as CO methanation catalysts due to their high activity, selectivity, and stability [9]. Although alloying Ni with Co can effectively inhibit metal sintering [10], the agglomeration of metal nanoparticles, and carbon deposition during exothermic reactions still limit their further development.

$$CO + 3H_2 \rightarrow CH_4 + H_2 \quad \Delta H_{298K} = -206.28 \quad kJ * mol^{-1} \tag{1}$$

$$2CO \rightarrow CO_2 + C \quad \Delta H_{298K} = -41.2 \quad kJ * mol^{-1} \tag{2}$$

Recent studies have shown that entropy plays a crucial role in structure-property relationships . At lower Gibbs free energy, strong system disorder and high structural randomness can contribute to enhancing the stability of host structures [11, 12]. The large number of homogeneously mixed and distributed metals in HEOs, can produce unexpected synergistic properties (cocktail effect). Due to the different surface charges of the multimetallic components, the surface charges of the multimetallic constituents redistribute in the HEOs, its d-band center can be easily adjusted by changing the composition of the element at the level of electronic structure [13]. In addition, significant lattice distortions occur within HEOs, increasing the number of oxygen vacancies as cations with

different radii are confined in the lattice. The increase in oxygen vacancies greatly improves the oxygen mobility of HEOs compared with conventional oxide supports, resulting in more active sites [14]. This multi-cation doped structure not only increases the oxygen vacancies but also reduces the energy of the catalytic system due to its high configurational entropy, which facilitates the activation and the mass transfer of the active metal [15].

Catalytic applications based on HEOs can be divided into two main categories [16]. The first is using HEOs directly as catalysts. Heterovalent cations that are stabilized by entropy create defects with unique properties that can alter the electronic properties. The second is using HEO as a stable carrier for anchor transitions and noble metal actives. High entropy oxides with enhanced molar configurational entropy, when used as catalysts, allows the dissolution of metals onto the sublattice to form strong metal-carrier interactions, which leads to efficient single-atom stabilization and high catalytic activity at high temperatures [17]. Zhao et al. [18] reported a Pt-HEO/Al_2O_3 catalyst prepared by a sol-gel-assisted mechanical milling method. The strong interaction between HEO and Al_2O_3 effectively inhibited the growth of HEO particles, leading to more surface defects, and the results showed that the catalyst not only possessed good hydrothermal aging stability but also long-term reactive stability for CO catalytic oxidation. Dai et al.[19] reported heterostructured, ultrastable $CuCeO_x$-$MgZnCoCuNiO_x$ catalysts prepared by a mechanochemical strategy, where $MgZnCoCuNiO_x$ HEO acted as a stabilizing reservoir, providing abundant Cu species that migrated through the oxide-oxide interface and formed a stable $CuCeO_x$ structure, exhibiting excellent high temperature stability, demonstrating the key role of entropy-induced structural remodeling at the oxide interface. Li et al. [20] elucidated the effect of oxygen vacancy density on the CO hydrogenation reaction through the prepared CuZnAlCeZrO HEO, and a higher surface oxygen vacancy concentration significantly enhanced the CO adsorption strength.

For the CO methanation process, the mechanism of hydrogen-assisted dissociation is well recognized, where the migration of hydrogen ions determines the reaction rate [21], and the large number of oxygen vacancies in HEOs can effectively promote hydrogen migration and enhance hydrogen overflow, thus increasing CO hydrogenation efficiency by increasing the density of the electron cloud of the metal and regulating the d-band center [22]. Based on the HEO's unique feature, it may be a feasible approach to develop efficient and stable catalysts in CO methanation. However, currently most of the HEO materials employed for thermal catalysis merely exploit the active

oxygen species for CO oxidation or combustion [23, 24]. The flexible combination of polymetallic components to achieve the high level of oxygen defects for the CO methanation process in HEOs has not yet been explored.

Among many crystal types, the spinel crystal type is preferred due to its good structural stability and sintering resistance [25, 26]. In addition, the selection of metal elements for HEOs catalysts should consider the similarity of ionic radii and crystal structures of the elements to ensure mutual solubility. In this study, the elements Cr and Mn, which have a strong preference for the spinel octahedral position, were selected not only to maintain the stability of the structure but also to facilitate the electron transfer and activation of the reactants [27]. Ni and Co elements with strong adsorption capacities for CO and H_2 were selected to enhance the catalyst activity [28]. Finally, the Al element with large differences in ionic radii from Ni, Co, Cr, and Mn are chosen to enhance the degree of lattice distortion. This is due to the localized stresses and distortions that occur when Al ions with smaller ionic radii replace larger ions in the lattice. This distortion breaks the symmetry of the lattice, which introduces more lattice defects and surface active sites [29, 30]. To ensure the purity and homogeneity of HEOs, it was prepared by the sol-gel method. Eventually, a new spinel-type HEO $(NiAlCoCrMn)_3O_4$ was synthesized. Meanwhile, according to the Hume-Rothery's rule [31], the stability of a solid solution depends on the similarity between solute and solvent ions, and the introduction of the element Al, which has a large difference in ionic radius, inevitably reduces the compatibility between the five metals [32], and the element Ni, which has a stronger tendency to the oxidation state of the +2-valence, is more susceptible to phase separation. Therefore, catalysts with different Ni contents were prepared by adjusting the Ni content, and the effects of Ni content on the phase separation, surface reconfiguration properties, and degree of oxygen defects of HEOs were investigated and validated by their performance in CO methanation reaction.

This study utilized a sol-gel method to synthesize a novel $(NiAlCoCrMn)_3O_4$ spinel-type HEO catalyst. The effect of Ni content on the physical phase and morphology of HEO was investigated through a series of characterizations, and its catalytic performance in the CO methanation reaction was evaluated using an independently built fixed-bed reactor. Finally, the mechanism for the excellent activity, selectivity, and stability of HEOs catalysts in the CO methanation reaction was analyzed in conjunction with the characterization results.

2. Experimental Section

2.1 Synthesis of HEOs Catalyst

The reagents used were of analytical grade without further purification. The reagents used in the experiment were all purchased from Aladdin Chemical Co. (China). Gas: Ar（≥99.99％），12%CO/ 40%H_2/ 48%Ar was purchased from Foshan Kodi Gas Chemical Industry Co, Ltd. $(NiAlCoCrMn)_3O_4$ HEO was prepared by the sol-gel method, as shown in Fig. 1. Specifically, 0.01 mol of $Co(NO_3)_2 \cdot 6H_2O$、$Cr(NO_3)_3 \cdot 9H_2O$, $Al(NO_3)_3 \cdot 9H_2O$, $Ni(NO_3)_2 \cdot 6H_2O$, and $Mn(NO_3)_2$ were dissolved in 20 ml of deionized water, then pour in a mixed solution of 0.1 mol citric acid (chelating agent), 0.001 mol PEG 4000 (surfactant) with 1.4 mol of solvent (ethylene glycol and n-butanol in a 1:1 molar ratio). The mixture was stirred at 90 °C for 12 h until it reached a sol-like state. The prepared wet gel was then dried in an oven at 120 °C for 48 h to obtain a dry gel. Afterward, the dry gel was calcined at 800 °C in a muffle furnace for 8 h and ground to obtain the $(NiAlCoCrMn)_3O_4$ sample. To investigate the effect of Ni content on the catalyst structure and catalytic performance, HEOs catalysts with different Ni contents were prepared using the same method, denoted as HEO-$Ni_{0.6}$, HEO-$Ni_{0.8}$, HEO-Ni_1, HEO-Ni_2, and HEO-Ni_3 with the molar ratios of Ni content relative to the other individual metal elements in the sample were 0.6:1, 0.8:1, 1:1, 2:1, and 3:1, respectively. In addition, in order to investigate the reason for the superior activity of HEOs compared to conventional catalysts, SiO_2 with an approximate specific surface area was used as an inert support. A bimetallic Ni-Co catalyst with a Ni: Co: Si molar ratio of 2:2:6 was prepared by wet impregnation as a control group. Firstly, 0.02 mol of $Ni(NO_3)_2 \cdot 6H_2O$ and $Co(NO_3)_2 \cdot 6H_2O$ were dissolved in 20 ml of deionized water at 60 °C with stirring, followed by the addition of 0.06 mol of nanosized SiO_2 (≧200 nm), which was continuously stirred for 1 h, and then dried for 12 h at 120 °C. Finally, after that, it was calcined at 500 °C under air for 4h and the sample obtained was labeled as $NiCo/SiO_2$.

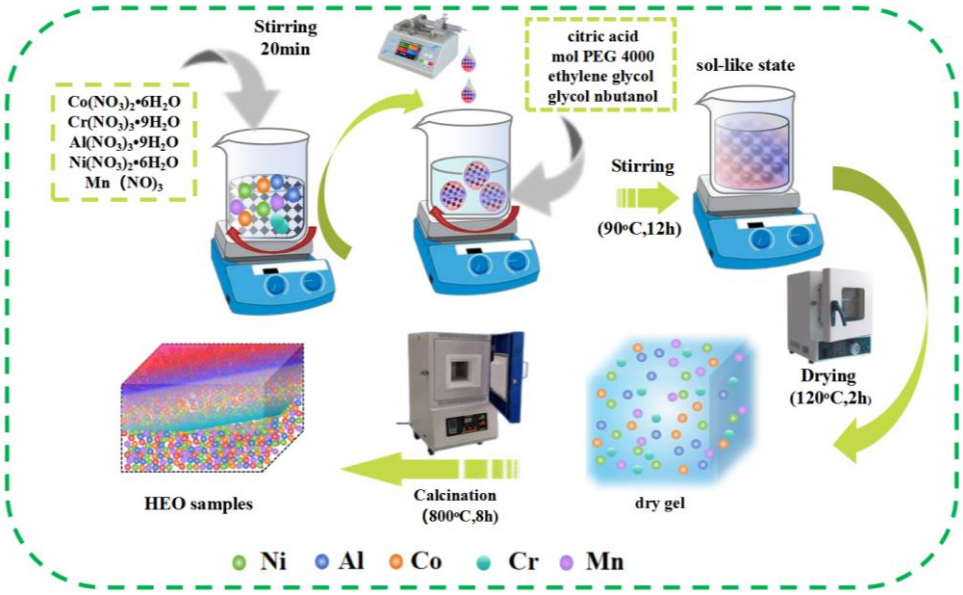

Fig. 1 Preparation of HEO by sol-gel method.

2.2 Catalyst characterization

In this study, X-ray diffraction (XRD) and in situ X-ray diffraction (in situ XRD) were used to analyze the crystalline phase structure of the samples using Rigaku XRD-Ultima IV and Anton Paar XRDynamic500, respectively, with a scanning speed of 2°/min to obtain more accurate crystallographic information. The particle sizes of metal oxides and alloys were calculated using the Scherrer equation [33]. Thermo Scientific K-Alpha X-ray Photoelectron Spectroscopy (XPS) was used to analyze the surface valence state distribution of oxygen in the samples. The binding energy of the peaks was corrected using the C1s peak centered at 284.6 eV. The surface morphologies of the samples were observed using a TESCAN MIRA LMS Scanning Electron Microscope (SEM), while microstructural images of HEOs were captured using a Thermo Scientific FEI Talos F200X Transmission Electron Microscope (TEM). Additionally, the elemental distributions of the samples were characterized using an Oxford Instruments X-Max Energy Dispersive X-ray Spectroscopy (EDS) system. The specific surface area and pore size information of the samples were obtained by N_2 adsorption-desorption studies using a Micromeritics ASAP2460 automatic surface area and the porosity analyzer. Hydrogen Temperature-Programmed Reduction (H_2-TPR), Hydrogen Temperature-Programmed Desorption (H_2-TPD) and CO pulse tests were performed using a Micromeritics Auto Chem II 2920 programmed warming chemisorption analyzer, and the gases were detected using a thermal conductivity detector (TCD). The carbon deposits of the samples were

investigated by thermogravimetric-differential thermal analysis (TG-DTA) using METTLER TOLEDO TGA/DSC 3+.

2.3 CO methanation experiments

The CO methanation experiment was conducted on a bench scale fixed-bed reactor shown in Fig. 2. A 0.3 g sample was placed in a quartz reaction tube with an inner diameter of 12 mm, and inert quartz support packing was filled at both ends of the sample. The quartz tube was placed in a reactor, and the temperature of the reactor was controlled by electric heating. Under Ar flow at 50 mL/min, the reactor temperature was ramped from room temperature to 600 ^{o}C at a heating rate of 10 ^{o}C/min. After stabilizing for 10 minutes, the gas flow was switched to a 150 ml/min H_2/Ar mixture gas (20% H_2) for reduction for 3 h. Subsequently, the reactor was cooled to the reaction temperature under Ar flow at 50 ml/min. After stabilizing for 2 minutes, the gas was switched to CO/H_2 (12% CO, 40% H_2, and 48% Ar) with a flow rate of 150 ml/min for the methanation reaction. After 60 minutes of the methanation reaction, the CO/H_2 mixture gas was shut off, and the reactor was cooled down under Ar flow protection to complete the experiment. The gas composition during the process was analyzed online using a gas chromatograph (GC-2014c, Shimadzu, Japan). The activity tests were conducted at 300-450 ^{o}C, and stability tests were conducted at 400 ^{o}C for 50 h. The definitions of CO conversion rate and methane selectivity are as follows:

$$\text{CO Conversion rate} = \frac{F_{(CO,in)} - F_{(CO,out)}}{F_{(CO,in)}} \times 100\% \quad (3)$$

$$\text{CH}_4\text{ Selective} = \frac{F_{(CH_4,out)}}{F_{(CO,in)} - F_{(CO,out)}} \times 100\% \quad (4)$$

In the formula, $F_{i(in/out)}$ represents the inlet/outlet flow rate of the reactor.

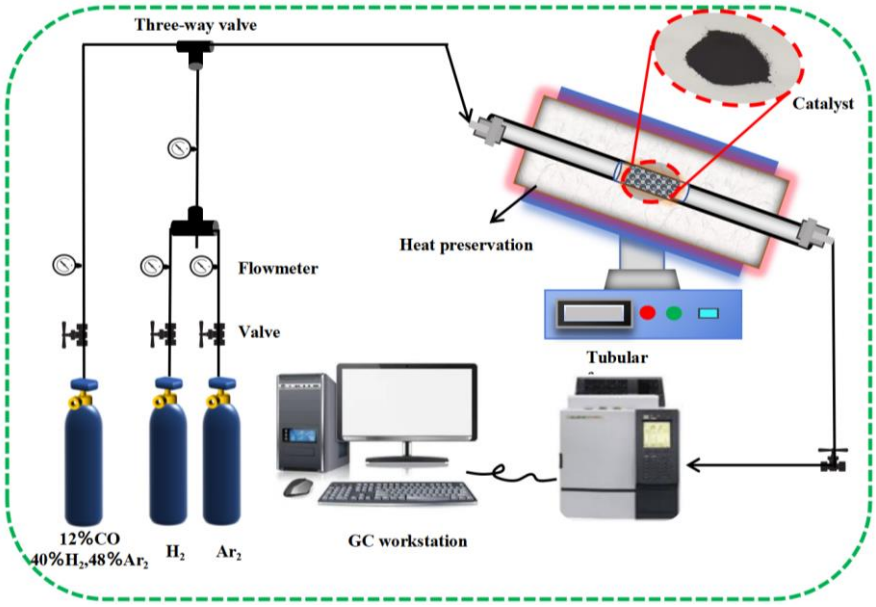

Fig. 2 CO methanation experiments.

3. Results and discussion

3.1 Characterizations of $(NiAlCoCrMn)_3O_4$

The XRD results of fresh samples with different Ni contents were shown in Fig. 3(a), where the characteristic peaks at 2θ=18.5˚, 30.5˚, 36.0˚, 37.7˚, 43.8˚, 54.4˚, 58.0˚, and 63.7˚ corresponded to the (111), (220), (311), (222), (400), (422), (511), and (440) planes of the spinel phase, indicating a spinel structure with AB_2O_4 composition, belonging to the Fd-3m (227) space group [34]. HEO-$Ni_{0.6}$ and HEO-$Ni_{0.8}$ exhibited only a single spinel phase structure. HEO-Ni_2 and HEO-Ni_3 exhibited additional peaks corresponding to NiO observed at (101), (100), and (220) reflections at 2θ=37.2˚, 43.2˚, and 62.9˚, respectively belonging to a Fm-3m space group. Moreover, the broadening of the NiO peaks in HEO-Ni_2 and HEO-Ni_3, with respective half-widths of 0.294 and 0.286, suggests an increase in crystallinity due to the higher Ni content. According to the Scherrer equation, the calculated NiO crystallite sizes for HEO-Ni_2 and HEO-Ni_3 are 29.3 and 37.1 nm, respectively.

As shown in the local enlargement of Fig. 3(a), whereas HEO-Ni_1 has an inconspicuous peak at the dashed line, which is connected to the diffraction peak at the crystallographic plane of spinel (222), (400). According to Gibb's energy [Eq. (5)], with increasing temperature and the number of elements, the single phase tends to stabilize because the configurational entropy counteracts the enthalpy controlled phase separation [35]. In order to determine whether there is a reversible transition of HEO-Ni_1 from a polyphase to a single phase, the dissolution of NiO into the spinel phase was

induced by lowering the Gibbs free energy by a sufficiently high temperature to increase the solubility of the solid.

$$\Delta G_{mix} = \Delta H_{mix} - T\Delta S_{mix} = \Delta H_{mix} + RT\sum_{i=1}^{n} x_i \ln(x_i) \quad (5)$$

With T= temperature, ΔH_{mix}= enthalpy of mixing, ΔG_{mix}= free enthalpy of mixing, R = universal gas constant, x_i= molar concentration of each component.

In situ XRD analysis of HEO-Ni_1 was carried out to investigate the presence of Ni monoxide species at high temperatures(Fig. 3(b)), As the temperature increases, the NiO (101), (100), and (220) diffraction peaks (2θ = 37.2˚, 43.2˚, 62.9) separated from those of the spinel and gradually move to a lower angle. According to Bragg's equation [36], this change is due to the expansion of the NiO lattice at high temperatures, resulting in a decrease in the diffraction angle, which leads to the separation of the diffraction peaks due to the difference in the lattice expansion rate between the different phases. When the temperature is reduced back to room temperature, the NiO diffraction peaks are re-covered by the spinel diffraction peaks, and this indicating phase separation occurs in HEO when 0.8 < x < 1.

XRD patterns of HEOs reduced in an H_2 atmosphere at 600 ºC is shown in Fig. 3(c). Compared to the fresh sample, HEO-$Ni_{0.8}$, HEO-Ni_1, HEO-Ni_2, and HEO-Ni_3 exhibit characteristic peaks at 2θ=44.5˚, 51.8˚, and 76.4˚, corresponding to the (111), (200), and (220) faces of NiCo alloy. The results show that HEO has surface reconfiguration properties in the reducing atmosphere and exsolves the NiCo alloy and is caused by the metal ions and oxygen ions in the equilibrium position of the HEO crystal migrating from their original positions to the crystal surface for establishing a new layer of ordered lattice structure known as the Schottky defect [37]. In contrast, no obvious NiCo metal peaks were found in HEO-$Ni_{0.6}$ after reduction. It is noteworthy that the diffraction peaks of the reduced spinel gradually broaden with increasing Ni content, which is attributed to the disruption of the spinel phase structure as well as more reactive metal covering the surface of the HEO, implying that high Ni content promotes surface reconfiguration of HEOs.

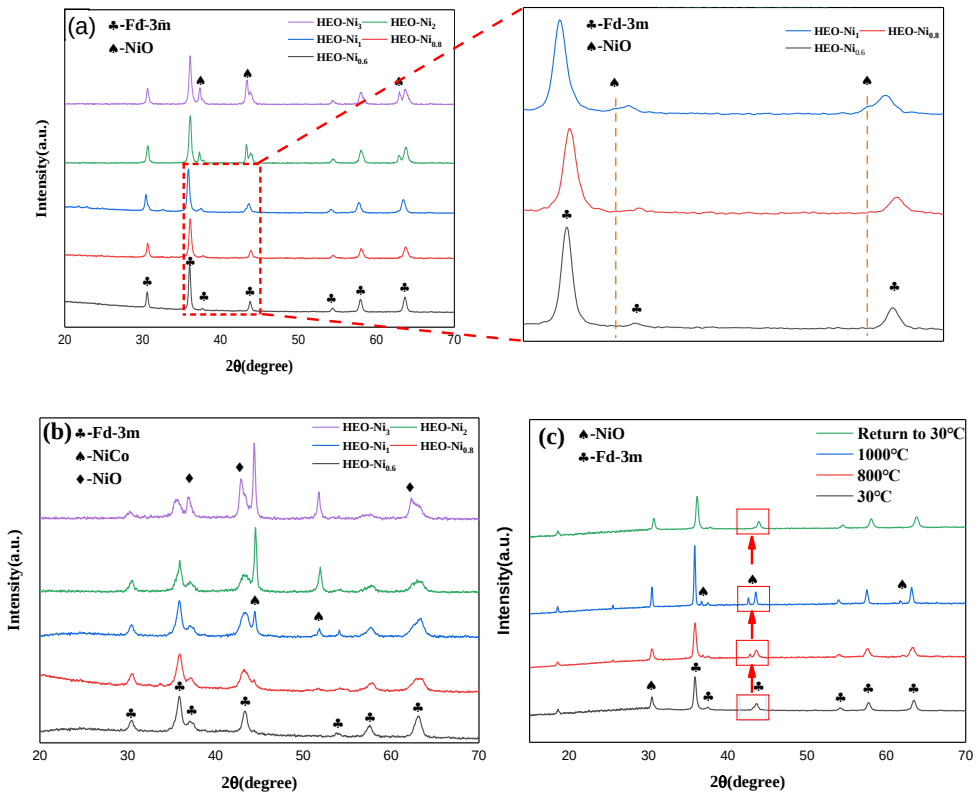

Fig. 3. (a) XRD diffraction patterns of fresh samples with different Ni contents and local magnified images, (b) In-situ XRD data diffraction patterns of HEO-Ni_1 at 30°C, 800°C, 1000°C, and after re-cooling to 30°C. (c) XRD of the reduced sample at 600 °C in H_2.

The samples with different Ni contents consisted of irregularly shaped aggregates (Fig. 4), with clear pore structures between the particles in all samples except HEO-Ni_2. This could be due to the formation of NiO particles of similar size to the pore diameter (29.3 nm) within the pores of HEO-Ni_2, which completely blocked the mesopores.

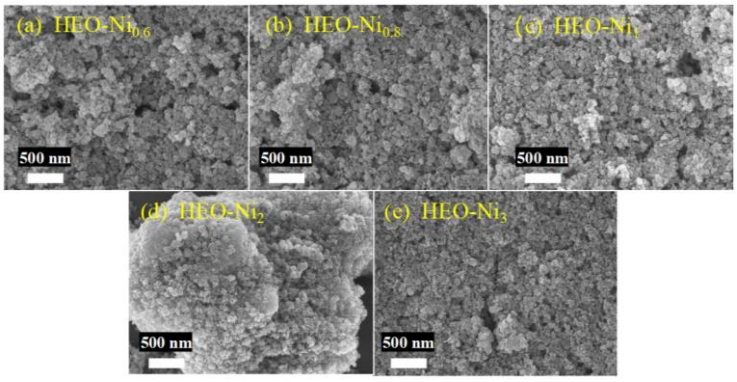

Fig. 4 The morphology of (a) HEO-$Ni_{0.6}$, (b) HEO-$Ni_{0.8}$, (c) HEO-Ni_1, (d) HEO-Ni_2, (e) HEO-Ni_3 under SEM.

The five metals Ni, Al, Co, Cr, and Mn are well dispersed on the micrometer scale (in Fig. 5), and there is no significant difference between the samples with different Ni contents. The elemental ratios were analyzed by SEM-EDS, as shown in Table 1. Except for HEO-Ni_2, the elemental molar ratios of the other samples roughly match the expected values. The lower Ni content in HEO-Ni_2 may be due to the formation of excess NiO particles, whose size is similar to the pores of HEO. Some NiO particles may reside within the HEO pores, beyond the detection depth of EDS, resulting in the lower measured content.

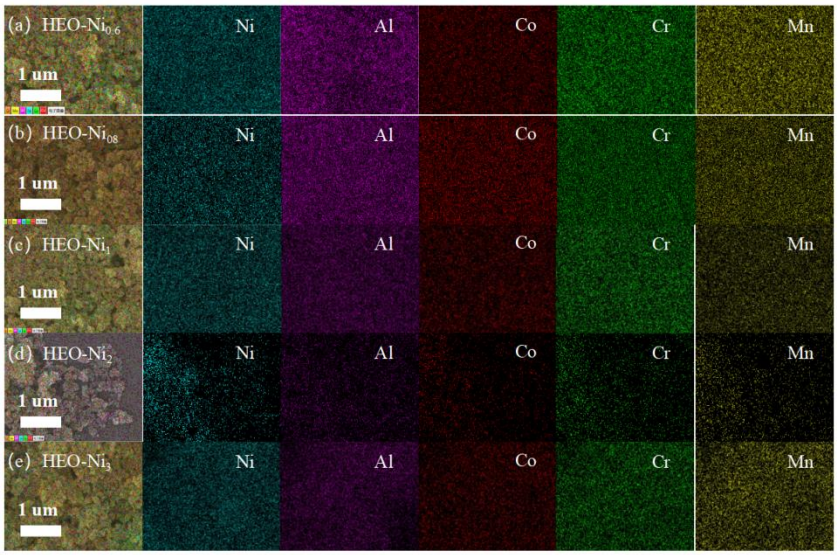

Fig. 5 HAADF-STEM image and corresponding EDX elemental mappings of (a) HEO-$Ni_{0.6}$, (b) HEO-$Ni_{0.8}$, (c) HEO-Ni_1, (d) HEO-Ni_2, (e) HEO-Ni_3 under SEM.

Table 1 SEM-EDS results for samples with different Ni content.

Samples	Ni (At%)	Al (At%)	Co (At%)	Cr (At%)	Mn (At%)
HEO- $Ni_{0.6}$	6.4	10.9	11.6	11.3	11.4
HEO- $Ni_{0.8}$	9.3	11.2	10.4	11.2	10.8
HEO- Ni_1	10.4	9.2	9.6	10.5	10.6
HEO- Ni_2	14.4	6.9	7.5	7.1	8.3
HEO- Ni_3	18.6	6.9	5.7	6.1	5.4

Fig. 6 illustrates the N_2 adsorption-desorption isotherms and the corresponding BJH pore size distribution plots for HEO-$Ni_{0.6}$, HEO-$Ni_{0.8}$, HEO-Ni_1, HEO-Ni_2, and HEO-Ni_3. As shown in Fig. 6(a), all three samples exhibited a typical type IV isotherm, with a noticeable H4 hysteresis loop at

$P/P_0 > 0.8$, indicating the presence of mesoporous structures, which is consistent with the SEM images. The BJH pore size distribution plots in Fig. 6(b) reveal that the pore sizes of all five samples predominantly cluster around 30 nm.

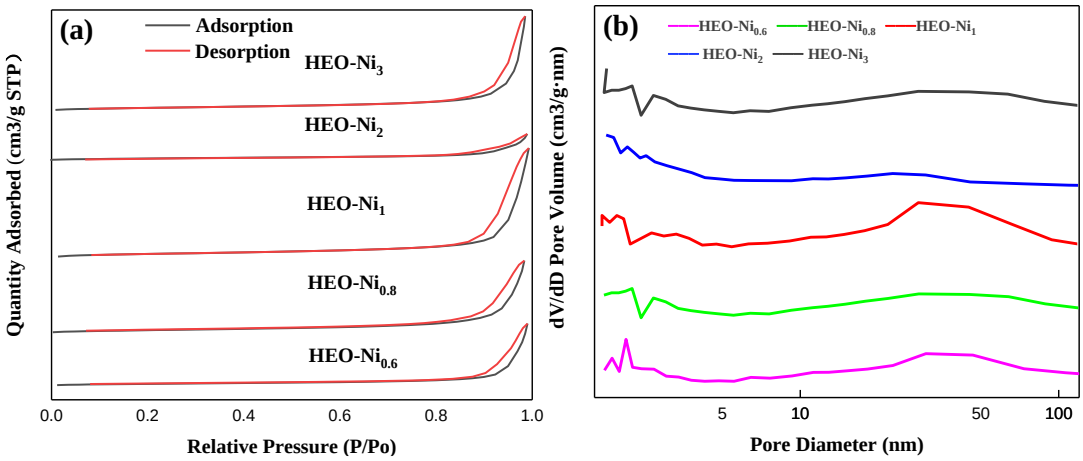

Fig. 6 (a) The N_2 adsorption-desorption isotherms and (b) the pore size plots distribution for fresh samples.

Table 2 summarizes the specific surface area, pore size, and pore volume for each sample. Initially, the specific surface area increases and then decreases with higher Ni content. This suggests that a moderate increase in Ni content may alter the local structure, leading to more defects, interfaces, and inhomogeneities, thus increasing the specific surface area of the catalyst [38]. However, excessive Ni can lead to NiO, which will form large particle clusters that cover the surface of the spinel support and block the catalyst pores. The remarkably low pore volume of HEO-Ni_2, at only 18.2118 cm^3/g, is due to the formation of NiO particles of similar size to the pore size (29.3 nm) within the pores, which completely blocks the mesopores. As shown in Fig. 4(d), a large number of pore structures were not found in the SEM image of HEO-Ni_2, so it has the lowest specific surface area of 7.032 m^2/g.

Table 2 Specific surface area, pore volume, and pore diameter of fresh samples.

Samples	Surface area (m^2 /g)	Pore volume (cm^3 /g)	Average pore size (nm)
HEO- $Ni_{0.6}$	9.540	0.078	32.790
HEO- $Ni_{0.8}$	13.470	0.090	26.730
HEO- Ni_1	17.850	0.133	29.950
HEO- Ni_2	7.030	0.032	18.210
HEO- Ni_3	13.810	0.116	33.720

Fig. 7 shows the microstructure of the fresh and reduced samples of HEO-Ni_1 to further understand the surface reconfiguration phenomenon. It was observed that HEO-Ni_1 consists of nanoparticles (NPs) with diameters less than 50 nm, and more than 75% of the NPs are in the range of 10-50 nm, which are stacked on top of each other due to the bridging effect to form a rich variety of different nanoscale channels (Fig. 7(a-b)). The pore size distribution data in Fig. 6b confirms this fact. The diversity of pore size channels not only promotes the diffusion of reactants and heat, but also provides a large internal surface area for H_2 and CO adsorption. The lattice spacing of 0.239 nm and 0.293 nm measured in the HRTEM images corresponding to (2 2 2) and (2 2 0) spinel crystal planes (Fig. 7(c)) is in agreement with the XRD results. All the elements of the catalyst were uniformly distributed on the nanoscale without significant bias, indicating that these elements were highly bound to each other (Fig. 7d). Fig. 7(e-g) shows the TEM image of HEO-Ni_1 after reduction. As shown in Fig. 7(e) it is evident that HEO-Ni_1 undergoes surface reconfiguration and precipitates metal particles from HEO, which grow on HEO with a size of around 6.76 nm. Lattice streaks belonging to the (1 1 1) and (2 0 0) crystal planes of NiCo alloys were measured in Fig. 7(g), identifying the metal particles as NiCo alloys, which is further confirmed by the EDS elemental mapping in Fig. 7(h). It is shown that the exsolved NiCo NPs was rooted in the bulk phase of HEO which matched well with the XRD results. Ni and Co cations distributed uniformly in the host HEO diffuse from the bulk phase to the surface and were reduced to form NiCo nanoalloy particles. Dissolved metal particles are embedded on the surface of HEO, showing a "semi-embedded-semi-exposed" heterogeneous interface state.

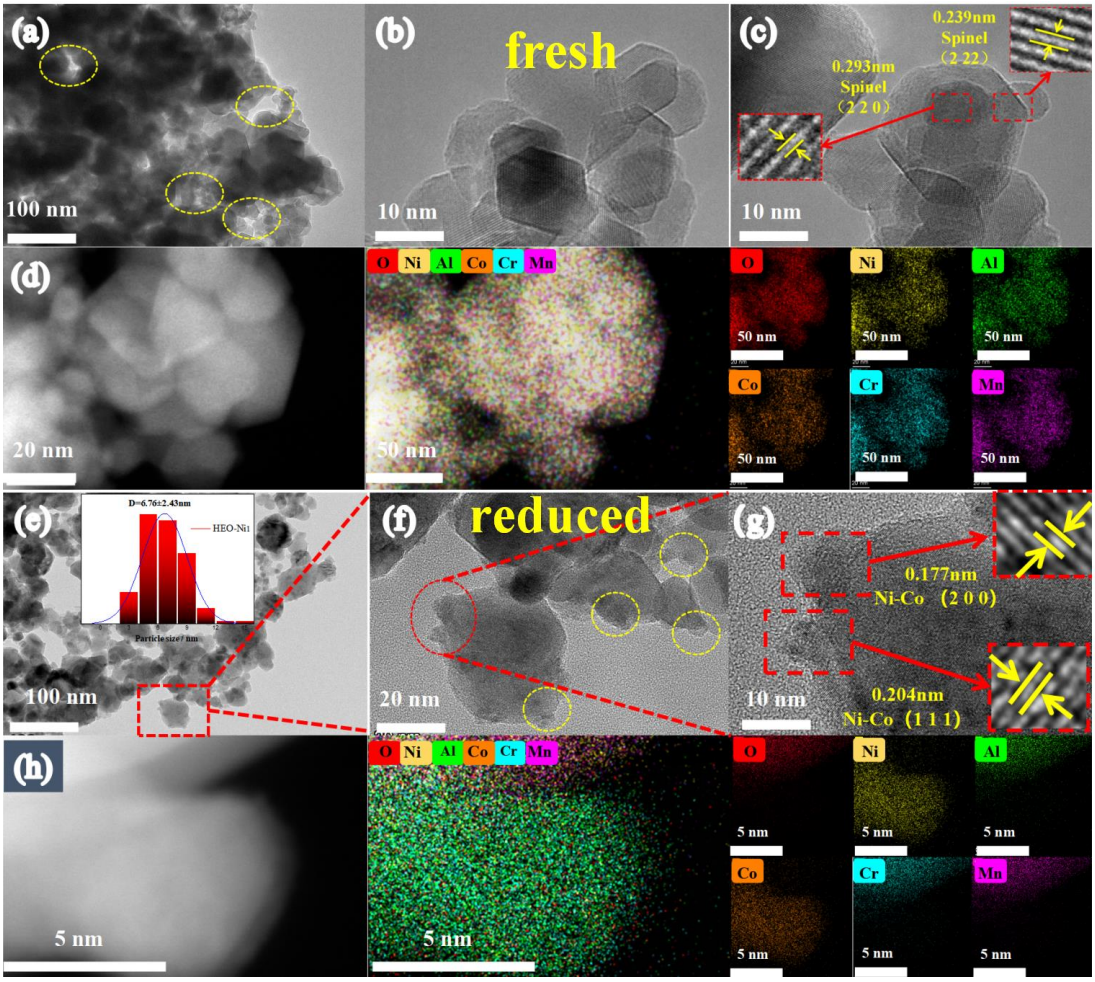

Fig. 7 Surface reconfiguration of HEO-Ni_1. Fresh sample: (a-c) TEM image, (d) HAADF-STEM image and corresponding EDS elemental mappings. Reduced sample: (e-g) TEM image, (h) HAADF-STEM image and corresponding EDS elemental mappings.

The reduction properties of HEO-$Ni_{0.6}$, HEO-$Ni_{0.8}$, HEO-Ni_1, HEO-Ni_2, and HEO-Ni_3 by H_2-TPR were analyzed .All five samples show distinct peaks in the 400-500 °C range shown in Fig. 8(a), which are the reduction peaks of strongly bound NiO on the surface of the spinel as well as Ni and Co ions within the spinel [39]. Ni and Co have similar electronegativities, lattice parameters, atomic radii , and similar crystal structures (face-centered cubic), allowing the two metals to form solid solutions with similar crystal structures according to the Hume-Rothery rule, forming highly homogeneous Ni-Co alloys [40]. The peak temperature and area are shown in Table 3. As the Ni content increases, the reduction peaks of Ni and Co ions inside the spinel solid solution gradually shift towards lower temperatures, and the peak area increases. This further suggests that the increase in Ni content reduced the temperature at the beginning of the surface reconfiguration process of

HEO. This may be because the increase in oxygen defects promotes the diffusion and adsorption behavior of hydrogen [41]. On the other hand, the peak area difference shows that the difference in Ni content between HEO-Ni_1 , HEO-Ni_2 and HEO-Ni_3 is reflected in the amount of NiO strongly bound to the support.

Table 3 Peak temperature and area of the five HEO samples reduction peaks.

Samples	Temperature at Maximum (°C)	Quantity (mmol/g)
HEO-$Ni_{0.6}$	467.10	0.37
HEO-$Ni_{0.8}$	463.29	0.46
HEO-Ni_1	444.51	0.61
HEO-Ni_2	436.20	1.12
HEO-Ni_3	432.45	2.32

Fig. 8 (b-c) shows the XPS spectra of before and after the reduction of HEO-$Ni_{0.6}$, HEO-$Ni_{0.8}$ and HEO-Ni_1 oxygen elements, the peaks of O1s at 529 eV, 530 eV, and 532 eV are respectively labeled as lattice oxygen (O_L), oxygen vacancies (O_V), and chemisorbed oxygen (O_C). The results are shown in Table 4, The O_V concentration of the fresh samples increased gradually with increasing Ni content and the O_V concentrations of HEO-$Ni_{0.6}$, HEO-$Ni_{0.8}$ and HEO-Ni_1 after reduction increased by 0.069, 0.089, 0.114. This could be attributed to the introduction of excess Ni, leading to the formation of more lattice defects or dislocations, and these defects could promote the generation of O_V under reduced conditions [42]. It is shown that the HEO surface reconfiguration process is accompanied by the generation of O_V and is facilitated by the increase in Ni content. In addition, the O elemental XPS spectra of the fresh/reduced NiCo/SiO_2 samples are shown in Fig. 8(d). Most of the surface O species belong to crystalline oxygen (Si-O) (532.9 eV) on SiO_2 supports [43], and the concentration of O_V is much lower than that of the three HEO samples, and the unchanged Si-O occupancy before and after reduction indicates that O_V belongs only to the oxygen deficiency on Ni and Co reactive metals. This is due to the high-entropy effect, which increases the tolerance for oxygen vacancies defects on the three HEO samples, as well as lattice distortions induced by different cation radii, which makes it easier to localize missing or removed oxygen atoms.

Table 4 O_V concentrations of HEO-$Ni_{0.6}$, HEO-$Ni_{0.8}$, HEO-Ni_1 and NiCo/SiO_2 samples before and after reduction.

Samples	O_V concentration of fresh samples	O_V concentration of reduced samples
HEO-$Ni_{0.6}$	0.27	0.34
HEO-$Ni_{0.8}$	0.33	0.42
HEO-Ni_1	0.42	0.53
NiCo/SiO_2	0.15	0.23

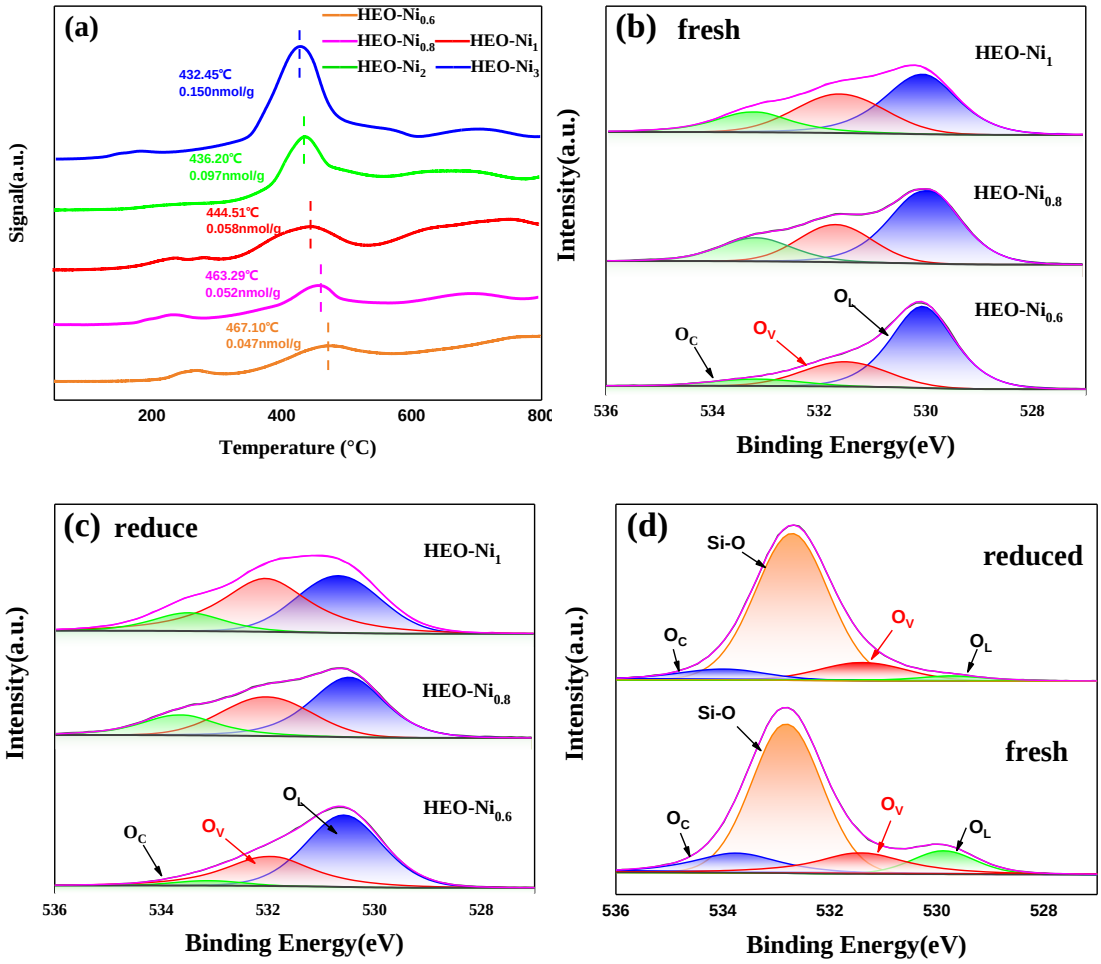

Fig. 8 (a) H_2-TPR curves of fresh samples of HEO-$Ni_{0.6}$, HEO-$Ni_{0.8}$, HEO-Ni_1, HEO-Ni_2, HEO-Ni_3. XPS spectra of HEO-$Ni_{0.6}$, HEO-$Ni_{0.8}$ and HEO-Ni_1 O1s. (b) fresh samples and (c) reduced samples. (d) XPS spectra of NiCo/SiO_2 O1s.

Fig. 9 summarizes the effect of Ni content on the surface self-reconfiguration of $(NiAlCoCrMn)_3O_4$ HEO. It shows the effect of Ni content on the solubility of NiCo NPs. With the increase in Ni content, more lattice oxygen is consumed and converted into oxygen vacancies, which

induces the reduction of more Ni and Co cations from the HEO bulk phase, and enhances the extent of the surface self-reconfiguration of the HEO, as indicated by the diffraction peaks of NiCo alloys in the XRD (Fig. 3b), the O1s in the XPS results, and the variation of hydrogen consumption in H_2-TPR (Fig. 8) is a strong proof of this deduction. The formation of O_V is a prerequisite for metal nucleation, which determines the amount of cation reduction in HEO. In a high-temperature reduction environment, the formation of O_V alters the pristine lattice of the host HEO, leading to localized dissolution of Ni and Co cations. In thermodynamic terms, the dissolution process is driven by the tendency to regenerate the thermodynamic steady state in the new environment. In a reductive atmosphere, the driving force for metal dissolution is the change in Gibbs free energy (▲G) from metal ions in the parent oxide to metal atoms. It is suggested that Co and Ni have high co-segregation energies (-0.55 eV and -0.50 eV) in oxides, which is conducive to the surface dissolution of NiCo alloy NPs [44].

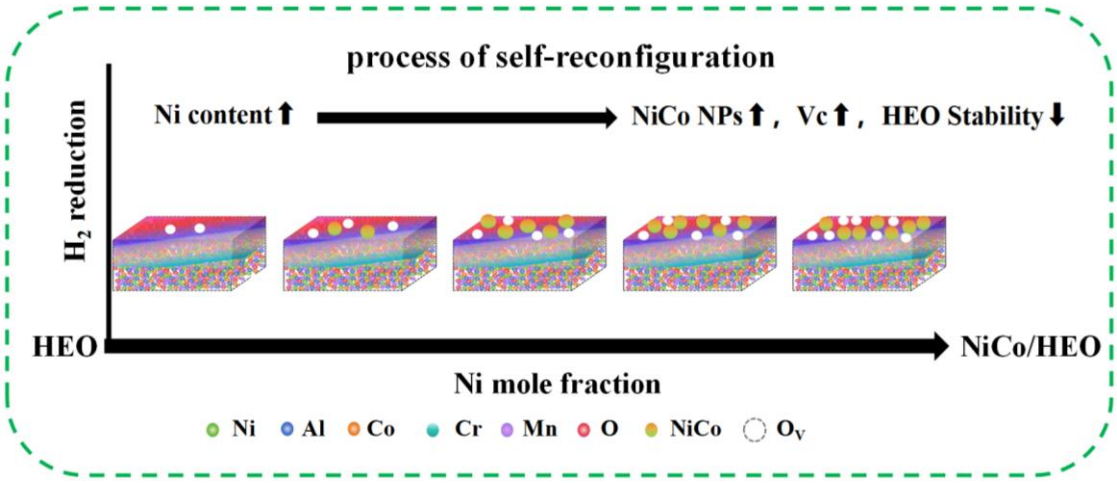

Fig. 9 Surface reconfiguration of HEO.

3.2 Catalyst CO Methanation Performance Test

In order to investigate the catalytic properties of HEO after surface reconfiguration. The catalytic activity of $NiCo/SiO_2$, HEO-$Ni_{0.6}$, HEO-$Ni_{0.8}$, HEO-Ni_1, HEO-Ni_2, and HEO-Ni_3 in the CO methanation process was tested at temperatures ranging from 300 to 450 °C. As observed in Fig. 10(a). The Ni content significantly influences the low-temperature CO conversion rate. As the temperature rises, the CO conversion rates of HEO-$Ni_{0.6}$ and HEO-$Ni_{0.8}$ gradually increase, reaching maximum values of 71.6% and 90.3% at 450 °C, respectively. HEO-Ni_1 and HEO-Ni_2 exhibit a

sharp increase from 300 °C, reaching maximum values of 99.56% and 96.6% at 400 °C, respectively. HEO-Ni_3, benefiting from its high Ni content, achieves a CO conversion rate of 99.4% at 300 °C and peaks at 99.69% at 375 °C. The lower conversion exhibited by HEO-Ni_2 is due to the lower specific surface area, resulting in a reduced number of active sites for the reaction. As shown in Fig. 10(b), the methane selectivity follows a similar trend as the CO conversion rate. At 400 °C, the methane selectivities of HEO-$Ni_{0.6}$, HEO-$Ni_{0.8}$, HEO-Ni_1, HEO-Ni_2, and HEO-Ni_3 are 74.0%, 84.9%, 85.9%, 77.3%, and 78.8%. The catalytic performance of the three samples, HEO-$Ni_{0.6}$, HEO-$Ni_{0.8}$, and HEO-Ni_1, showed significant differences. In addition to the influence of the active components, the concentration of O_V was also an important factor. As shown in insert Fig. 10(a-1) and 10(b-1), with the increase of O_V concentration plus, the catalysts showed a rapid increase in CO conversion and CH_4 selectivity at 400 °C, which was attributed to the presence of O_V. The O_V can provide additional adsorption sites on the carrier surface, increasing the opportunity for CO molecules to contact the catalyst surface. It can also regulate the adsorption capacity and activation energy of CO molecules by changing the electronic state on the catalyst surface, which is conducive to promoting the adsorption and reducing the activation barrier for CO hydrogenation, thus improving the CO methanation performance[45, 46].

The lower CH_4 selectivity of HEO-Ni_2, and of HEO-Ni_3 is attributed to the fact that the active component of HEO-Ni_2, and of HEO-Ni_3 consists of two parts, Ni formed after NiO reduction and NiCo alloys precipitated by HEO, with a part of the hydrogenation reaction being carried out on the monometallic Ni, which makes them more active at low temperatures, but relative to the NiCo alloys, the lower CO adsorption dissociation capacity makes it more difficult to break the C-O bond and reduces the CH_4 selectivity in general [47]. The lowest CH_4 selectivity of HEO-$Ni_{0.6}$ low may be due to the fact that the small number of active components spilled on the surface is not enough to form a stable alloy phase, but the monometallic component acts as a catalyst [48].

The catalytic stability experiments of NiCo/SiO_2, HEO-Ni_1 and HEO-Ni_3 were carried out for 50 h. Fig. 10(c) illustrates the changes in CO conversion and CH_4 selectivity over time. The conversion of HEO-Ni_3 decreased rapidly from 99.4% to 75% within 30 h. In contrast, HEO-Ni_1 exhibited no significant decrease, stabilizing at 98% or above, and the conversion gradually increased over time from 98.92% to 99.81% within the first 15 h. This trend can be attributed to the surface reconfiguration of HEOs is still in progress under the reducing atmosphere of CO/H_2,

leading to the formation of more active sites. The trend of CH_4 selectivity over time is the same as that of CO conversion, and the CH_4 selectivity of HEO-Ni_1 and HEO-Ni_3 is stabilized at 83% and 74%.

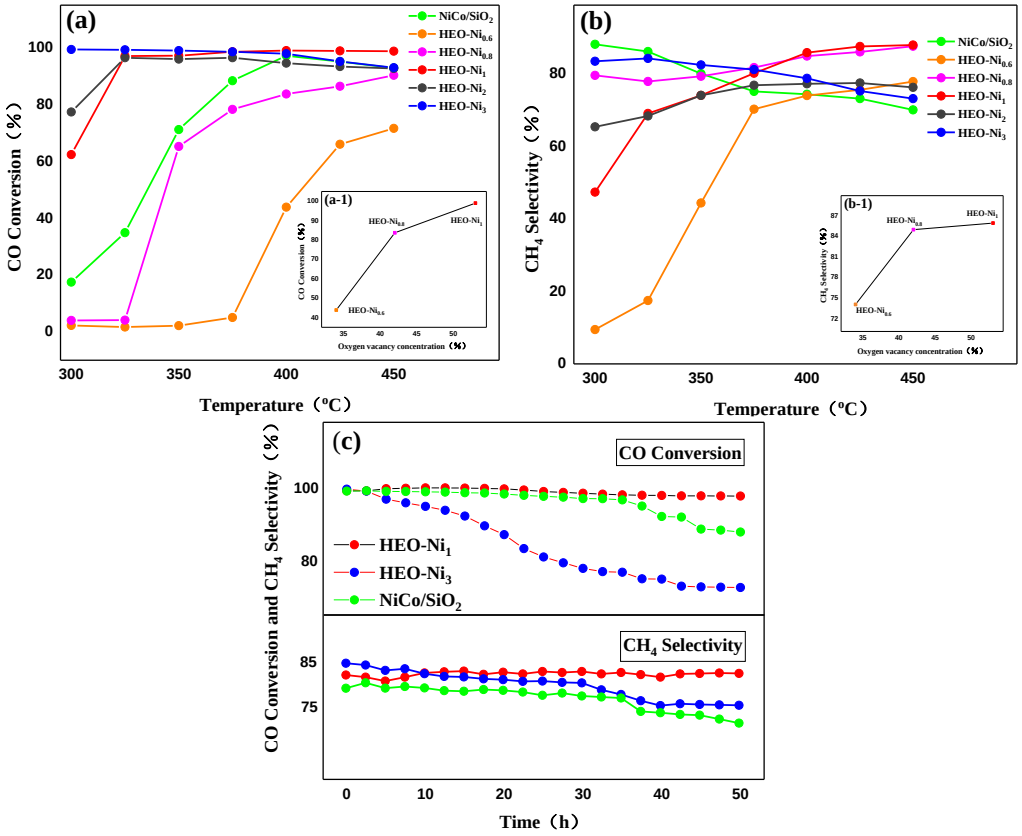

Fig. 10 The performance tests of the catalysts: $NiCo/SiO_2$, HEO-$Ni_{0.6}$, HEO-$Ni_{0.8}$, HEO-Ni_1, HEO-Ni_2, and HEO-Ni_3, for (a) CO conversion rate, and (b) CH_4 selectivity at 300-450 °C. The inserted figures show the variation of (a-1) CO conversion rate and (b-1) CH_4 conversion rate with oxygen vacancy concentration of the catalyst at 400°C. (c) The variations in CO conversion rate and CH_4 selectivity over time for HEO-Ni_1 and HEO-Ni_3 at 400 °C.

The performance test results were as expected, the moderate increase of Ni content enhances the surface reconfiguration process of HEOs, and the dissolution of more Ni and Co ions forms NiCo alloys as active sites, which effectively improves the CO conversion rate. But the performance of HEO-Ni_3 in the stability test was not as good as expected. In order to investigate the reason, the spent samples of HEO-Ni and HEO-Ni_3 were analyzed by TEM/EDS elemental mapping, XRD, TG, SEM, and TEM/EDS elemental mapping characterization.

Fig. 11(a) shows XRD maps of HEO-Ni_1 and HEO-Ni_3 waste samples, which indicates that the half-peak widths of both HEO-Ni_1 and HEO-Ni_3 metal NiCo in the (1 1 1) phase plane (2θ= 44.5°) decrease and the heights of the spinel diffraction peaks decrease as compared to the reduced ones, suggesting that the surface reconfiguration of HEO under the reaction atmosphere is still continuing, confirmed by the gradual increase in the conversion of HEO-Ni_1 at the beginning of the stability test. Subsequently, TG tests were performed on HEO-Ni_1 and HEO-Ni_3 spent catalysts under air atmosphere. As shown in Fig. 11(b), the weight loss of HEO-Ni_1 and HEO-Ni_3 below 225 °C was due to the evaporation of adsorbed H_2O on the sample surface. The samples gained 3.05% and 5.91% of weight at 225~700 °C, respectively, owing to the oxidation of Ni-Co alloys and carbon buildup. To determine the degree of carbon deposition, the carbon deposition behavior of HEO-Ni_1 and HEO-Ni_3 was further evaluated by SEMEDS. As shown in the insets (b-1) and (b-2) in Fig. 11(b), the HEO-Ni_1 and HEO-Ni_3 particles maintained the particle stacking morphology after the reaction, and the surface structures of the two samples were not damaged after a long time of treatment. The contents of HEO-Ni_1 and HEO-Ni_3 carbon deposition were 1.9 wt% and 5.7 wt%, respectively, and HEO-Ni_1 had a better carbon deposited resistance than that of HEO-Ni_3, which was attributed to the smaller NiCo alloy particle size and the large specific surface area. Meanwhile, it can be deduced from the mass loss of oxygen atoms lost by NiO combined with the ratio of TG weight gain of the two samples to the carbon weight ratio of the accumulated carbon that the ratio of oxygen atoms lost by HEO-Ni_1 and HEO-Ni_3 belonging to the surface reconfiguration of HEO is 4.95:6.6, which further confirms that the increase in the content of Ni promotes the surface reconfiguration of HEOs.

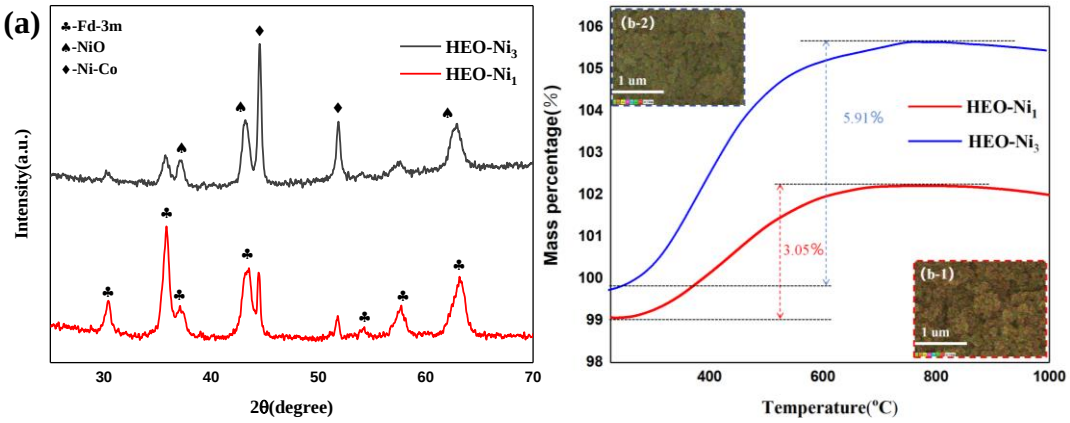

Fig. 11 HEO-Ni_1, HEO-Ni_3 spent catalysts (a) XRD, (b) TG curves and inserted SEM images: (b-1) HEO-Ni_1, (b-2) HEO-Ni_3.

Fig. 12 shows the TEM and HAADF-STEM mapping images of HEO-Ni_1 and HEO-Ni_3 spent samples. Lattice streaks belonging to the NiCo alloy (1 1 1) and (2 0 0) crystal planes were measured in the TEM images of both samples (Fig. 12(a), (c)). Among them, the (1 1 1) crystal surface of NiCo alloys has a lower C hydrogenation barrier relative to Ni and Co monometallics, which is beneficial for improving the activity and selectivity of the CO methanation reaction [49]. In Fig. 12(a) it is observed that the NiCo alloy of HEO-Ni_1 has an average particle size of 6.88 nm which is approximately the same as before the reaction, and grows uniformly on the surface of the spinel, and no particle agglomeration is found. In Fig. 12(b) the NiCo alloy of HEO-Ni_3 has an average particle size of 18.02 nm, which is due to the migration and agglomeration of particles. Combined with the XRD diagrams before and after HEO reduction, it shows that although the high Ni content promotes the surface reconfiguration of HEOs so that more active metal exsolution increases the active sites, it also decreases the stability of the support structure, which is not conducive to the anchoring of the active metal to the support, and increases the risk of the active metal agglomeration. In the EDS mapping images of the two samples, no other elements are present in the region where Ni and Co elements are clustered, while in the other regions, the five metal elements are uniformly distributed with the O elements, and the results demonstrate that HEO is transformed into NiCo/HEO high-entropy loaded catalyst after surface reconfiguration.

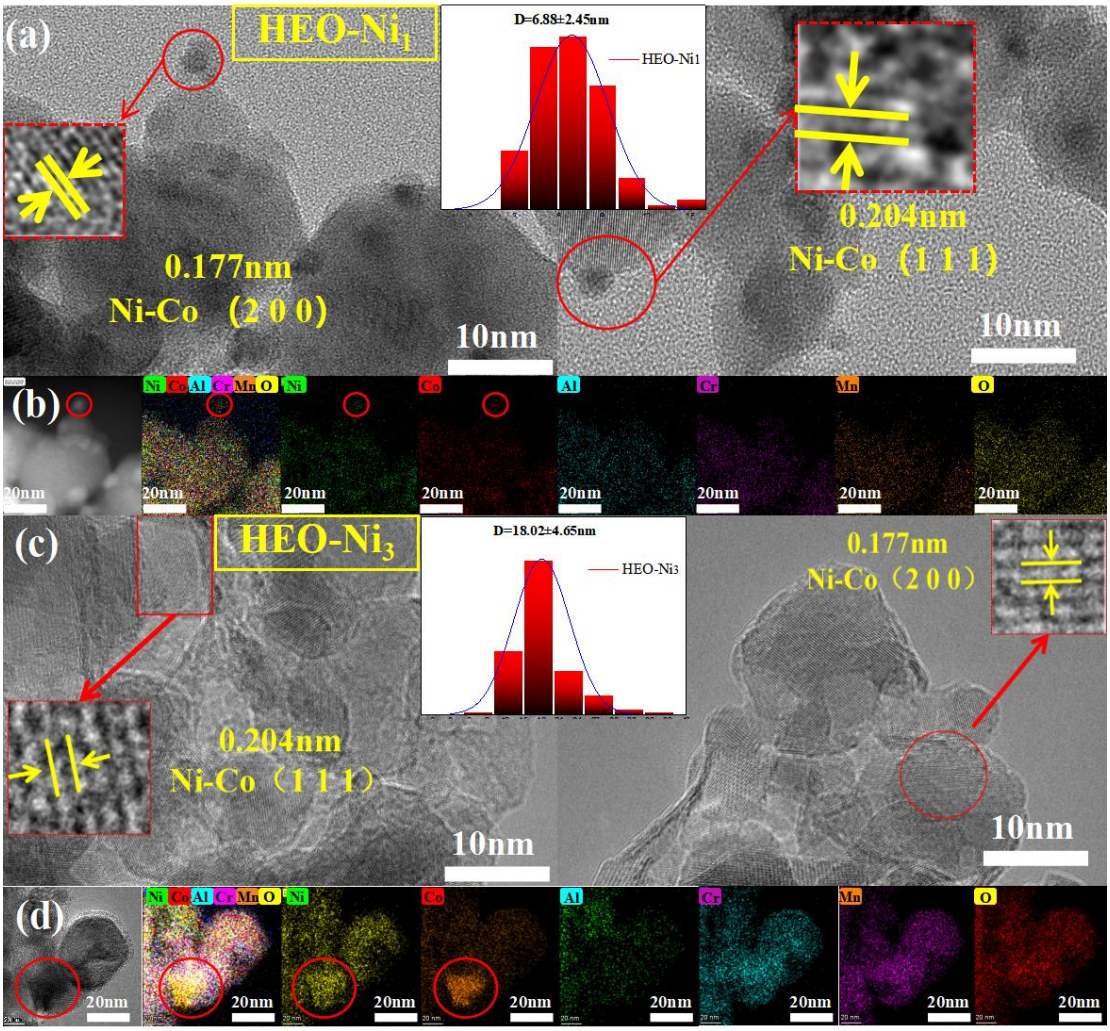

Fig. 12 (a) TEM image, HAADF-STEM image and (b) corresponding EDS elemental mappings of HEO-Ni_1 spent sample. (c) and (d) for HEO-Ni_3 spent sample, respectively.

Compared to the inert support $NiCo/SiO_2$, HEO-Ni_1 with the same content of Ni and Co has a wider active temperature range and higher CH_4 selectivity, especially at low temperatures. The CO conversion was 97.1% and 98.8% at 325 and 450, respectively, compared with only 34.9% and 92.9% for $NiCo/SiO_2$. At the same time, HEO-Ni had better stability, and the CO conversion rate only decreased by 1.6% after 50 h measurement, while $NiCo/SiO_2$ decreased by 12.6% (Fig. 10). Unlike the $NiCo/SiO_2$ impregnation method for loading Ni and Co bimetallics, as seen from the TEM image of Fig. 12 HEO-Ni_1, the Ni and Co ions exsolved from within HEO form a highly homogeneous NiCo alloy, and the strong interactions between them form an electron-rich metal surface, which not only promotes adsorption of CO, but also weakens the C-O bond and leads to C-O breakage, thus improving the CO conversion efficiency [50].

The results of CO pulse tests on HEO-Ni_1 and $NiCo/SiO_2$ are shown in Fig. 13(a). As shown, the adsorption amounts of HEO-Ni_1 and $NiCo/SiO_2$ were 0.02472 mmol/g and 0.01722 mmol/g, respectively, and the larger CO adsorption amount with fewer pulses proves that HEO-Ni_1 has a stronger adsorption capacity for CO. This is related to the significant O_V concentration difference on the surfaces of HEO-Ni_1 and $NiCo/SiO_2$, and the presence of O_V enhances the adsorption capacity of the active sites for CO, thereby increasing the CO adsorption rate. In addition, good metal dispersion can provide more active sites, and the metal dispersion was calculated to be 66.08% and 3.89%, respectively. This is due to the fact that the NiCo alloy in HEO-Ni_1 is exsolved from the HEO solid solution with a highly homogeneous elemental distribution by surface reconfiguration. The large number of O_V on HEO is also responsible for the excellent CO methanation performance of HEO-Ni_1. The large number of oxygen vacancy sites promotes the breaking of the O-C bond of CH_3O and reduces the possibility of CH_3OH generation [21], and this is consistent with the results of tests for CH_4 selectivity.

In addition, CO undergoes stepwise hydrogenation to form CHO and the resultant CHO hydrogenates to CH_2O. The CH_2O further undergoes stepwise hydrogenation to form CH_3O, which then dissociates into CH_3. CH_4 formation can easily happen according to CH_3 hydrogenation [51]. Therefore, the ability of H migration indirectly determines the activity of CO methanation. As Fig. 13(b), the H_2-TPD curve of HEO-Ni_1 has three peaks and a large amount of hydrogen desorption in the range of 350-600 °C, and the resolution peaks around 140 °C and after 700 °C are attributed to the weak versus strong desorption of hydrogen to the active metal sites. HEO-Ni_1 has more hydrogen desorption compared to $NiCo/SiO_2$ at low temperatures, which is probably due to the anti-synergistic effect of NiCo alloys as well as the presence of O_V weakening the interaction between NiCo alloys and H^+ [52] and decreasing the adsorption capacity for H_2. The weaker H-binding indicates higher hydrogen surface mobility, which not only promotes hydrogenation and reduces carbon deposition, but also alleviates the competing desorption of CO and H_2 during the CO methanation reaction [53]. And the hydrogen desorption peak at 350-600 °C is attributed to the reverse spillover of H_2 from HEO to NiCo alloy [54]. The hydrogen desorption peak at 200-350 °C is attributed to the desorption of H_2 adsorbed by HEO as shown in Fig. 13(c) with an oscillating curve within 200-350 °C, which confirms the competing process of H_2 adsorption-desorption by HEO. This is

attributed to the large number of O_V on HEO that enhance the chemisorption of H_2 [55]. In contrast, $NiCo/SiO_2$ did not show a significant hydrogen desorption peak in the range of 350-600 °C.

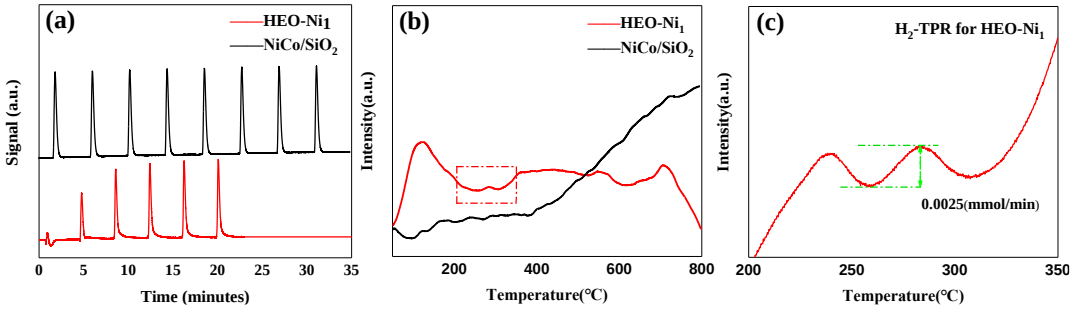

Fig. 13 (a) CO Pulse Chemisorption Curve and (b) H_2-TPD Curve for reduced HEO-Ni_1 and with $NiCo/SiO_2$, (c) H_2-TPR for HEO-Ni_1.

Fig. 14 summarizes the synergistic effect of massive oxygen defects on the surface of HEO and a homogeneous NiCo alloy. The large amount of O_v on the surface of HEO and the exsolved NiCo alloy play complementary roles in the CO hydrogenation reaction, the NiCo alloy with weak adsorption of H_2 provides a site not only for the transfer of H^+ but also slows down the competition between the adsorption of H_2 and CO. The HEO, which possesses a large amount of Ov on its surface, acts as a support and serves to store hydrogen. The fluctuation curves of the H_2-TPR and the H_2 resolution peak of H_2-TPD 350-600 ºC indicate that The HEO support with a large number of O_v not only adsorbs H directly from the external environment, but also accepts H from the hydrogen overflow from NiCo alloy and provides a hydrogen source for the carbon buildup on NiCo alloy through the reverse hydrogen overflow, thus avoiding catalyst deactivation due to carbon deposition. In addition, exsolved metal particles are embedded on the surface of HEO, showing a "semi-embedded-semi-exposed" heterogeneous interface state, and the HEO acts as an anchor for the NiCo alloy exsolved from the HEO, limiting the migration of the NiCo alloy, and avoiding agglomeration, so that the dimensions of the NiCo alloys on the HEO samples remain almost unchanged after a long reaction time.

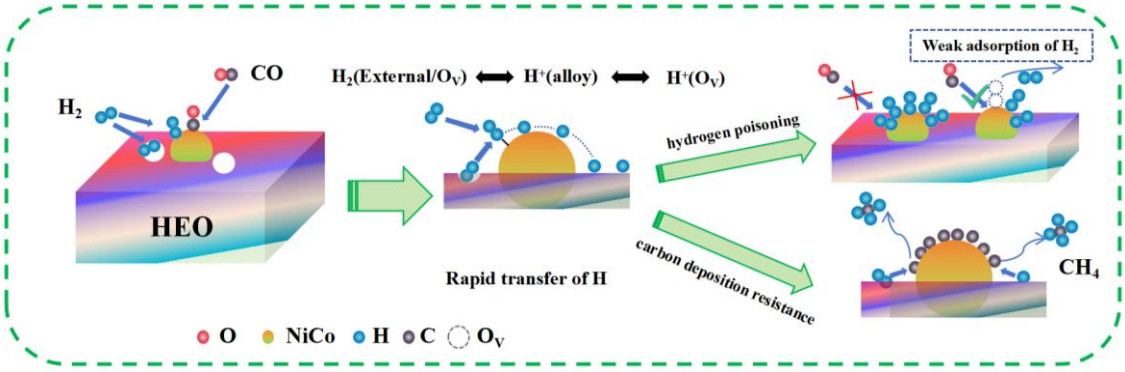

Fig.14 Catalytic effect of NiCo/HEO on CO methanation.

4. Conclusion

In this paper, a new type of high-entropy spinel $(NiAlCoCrMn)_3O_4$ catalyst was prepared by the sol-gel method with different Ni contents, and it was found that when there was a phase separation within the range of $0.8<x<1$. The self-reconfiguration property of $(NiAlCoCrMn)_3O_4$ leads to the redistribution of Ni and Co ions inside the HEO and the formation of uniformly dispersed NiCo alloys on the HEO surface, and the increase in Ni content promotes this behavior. But too high Ni content formed large particles of NiO, which led to the blockage of pores and the sintering of NiCo alloy, and reduced the catalytic performance.

In addition, the NiCo/HEO formed after surface self-reconfiguration has an unexpected metal-support synergy. In addition to the stable structure of the HEO acting as a support, which restricts the migration of the NiCo alloy, HEO with large number of O_V can also act as a hydrogen storage layer, which can provide an additional source of hydrogen for the active sites of the NiCo alloy when needed, and reduce the possibility of carbon accumulation. The weak adsorption of H_2 by the uniformly dispersed NiCo alloy not only provides good hydrogen transfer capability, but also avoids the adsorption of a larger amount of H_2, which provides good CO methanation activity and high-temperature stability. The NiCo/HEO catalysts formed by HEO-Ni_1 after surface self-reconfiguration had a CO conversion of 99% and a methane selectivity of 87% at 400 °C. This study provides a reference for new applications of HEOs in thermal catalysis.

Acknowledgments

This work was supported by National Key Research and Development Plan (No. 2022YFE0198800), Natural Science Foundation of China (NO. 22378073).

5. References:

1 G. C. Leung, *Handbook of clean energy systems* **2015**, 1-15.

2 B. C. Steele, *Nature* **1999**, *400*, 619-621.

3 Y. Li, Q. Zhang, R. Chai, G. Zhao, Y. Liu, Y. Lu, *ChemCatChem* **2015**, *7*, 1427-1431.

4 I. Hussain, A. Jalil, N. Hassan, M. Farooq, M. Mujtaba, M. Hamid, H. Sharif, W. Nabgan, M. Aziz, A. Owgi, *Fuel* **2022**, *311*, 122604.

5 S. Rönsch, J. Schneider, S. Matthischke, M. Schlüter, M. Götz, J. Lefebvre, P. Prabhakaran, S. Bajohr, *Fuel* **2016**, *166*, 276-296.

6 L. Gómez, G. Grasa, I. Martínez, R. Murillo, *Chemical Engineering Science* **2023**, *267*, 118291.

7 J. Barrientos, M. Lualdi, M. Boutonnet, S. Järås, *Applied Catalysis A: General* **2014**, *486*, 143-149.

8 B. Miao, S. S. K. Ma, X. Wang, H. Su, S. H. Chan, *Catalysis Science & Technology* **2016**, *6*, 4048-4058.

9 J. Gao, Q. Liu, F. Gu, B. Liu, Z. Zhong, F. Su, *Rsc Advances* **2015**, *5*, 22759-22776.

10 W. Tang, J.-P. Cao, C.-C. Chen, W. Jiang, C.-X. Chen, Z.-M. He, K.-R. Luan, X.-Y. Zhao, *Chemical Engineering Science* **2023**, *281*, 119165.

11 S. H. Chung, Y. H. Wu, Y. H. Tseng, T. X. Nguyen, J. M. Ting, *ChemSusChem* **2023**, *16*, e202300135.

12 H. Chen, J. Fu, P. Zhang, H. Peng, C. W. Abney, K. Jie, X. Liu, M. Chi, S. Dai, *Journal of Materials Chemistry A* **2018**, *6*, 11129-11133.

13 M. Theibault, C. R. McCormick, S. Lang, R. E. Schaak, H. D. Abruña, *ACS nano* **2023**, *17*, 18402-18410.

14 S. H. Albedwawi, A. AlJaberi, G. N. Haidemenopoulos, K. Polychronopoulou, *Materials & Design* **2021**, *202*, 109534.

15 A. Sarkar, L. Velasco, D. Wang, Q. Wang, G. Talasila, L. de Biasi, C. Kubel, T. Brezesinski, S. S. Bhattacharya, H. Hahn, B. Breitung, *Nat Commun* **2018**, *9*, 3400 10.1038/s41467-018-05774-5.

16 Y. Sun, S. Dai, *Science Advances* **2021**, *7(20)*, eabg1600.

17 P. Yin, S. Hu, K. Qian, Z. Wei, L. Zhang, Y. Lin, W. Huang, H. Xiong, WX. Li, HW. Liang, *Nature Communications*, **2021**, *12(1)*, 4865.

18 S. Zhao, J. Lin, P. Wu, C. Ye, Y. Li, A. Li, X. Jin, Y. Zhao, G. Chen, Y. Qiu, D. Ye, *ACS Applied Materials & Interfaces*, **2021**, *13(41)*, 48764-48773.

19 H. Chen, K. Jie, CJ. Jafta, Z. Yang, S. Yao, M. Liu, Z. Zhang, J. Liu, M. Chi, J. Fu, S. Dai, *Applied Catalysis B: Environmental*, **2020**, *276*, 119155.

20 J. Li, X. Yuan, F. Tian, M. Wang, T. Hu, G. Xiong, X. Wang, *Applied Catalysis A: General*, **2024**, *681*, 119781.

21 J.-M. Kim, S.-H. Kim, S.-Y. Park, S.-S. Kim, S.-J. Lee, *Chemical Engineering Science* **2019**, *209*, 115219.

22 X. Han, J. Yang, B. Han, W. Sun, *international journal of hydrogen energy* **2017**, *42*, 177-192.

23 F. Okejiri, Z. Zhang, J. Liu, M. Liu, S. Yang, S. Dai, *ChemSusChem* **2020**, *13*, 111-115.

24 Y. Gao, Y. Liu, H. Yu, D. Zou, *Applied Catalysis A: General* **2022**, *631*, 118478.

25 Y. Liu, S. Qing, X. Hou, F. Qin, X. Wang, Z. Gao, H. Xiang, *ChemCatChem* **2018**, *10*, 5698-5706.

26 S. Dey, G. C. Dhal, Materials Science for Energy Technologies **2019**, 2, 575-588.

27 A. Purwanto, A. Fajar, H. Mugirahardjo, J. Fergus, K. Wang, *Journal of Applied Crystallography* **2010**, *43*, 394-400.

28 J. Rabo, A. Risch, M. Poutsma, *Journal of Catalysis* **1978**, *53*, 295-311.
29 T. He, L. Chen, Y. Su, Y. Lu, L. Bao, G. Chen, Q. Zhang, S. Chen, F. Wu, *Journal of Power Sources*, **2019**, *441*, 227195.
30 X. Hua, X. Mao, S. Yang, M. Zhang, L. Fu, C. Han, A. Huang, H. Gu, *Journal of Alloys and Compounds*, **2024**, *994*, 174631.
31 S. Choudhury, JA. Aguiar, MJ. Fluss, LL. Hsiung, A. Misra & BP. Uberuaga, *Scientific reports*, **2015**, *5(1)*, 13086.
32 M. Fracchia, M. Coduri, P. Ghigna, U. Anselmi-Tamburini, *Journal of the European Ceramic Society*, **2024**, *44*, 585-59433.
33. A. Monshi, M. R. Foroughi, M. R. Monshi, *World journal of nano science and engineering* **2012**, *2*, 154-160.
34 GM Tomboc, X Zhang, S Choi, D Kim, L. Lee, S. Y. L, K. LEE, *Advanced Functional Materials,* **2022**, 32(43), 2205142.
35 CM. Rost, E. Sachet, T. Borman, A. Moballegh, EC. Dickey, D. Hou, JL. Jones, S. Curtarolo, J. P. Maria, *Nature communications*, **2015**, *6(1)*, 8485.
36 A. Fantin, G. O. Lepore, A. M. Manzoni, S. Kasatikov, T. Scherb, T. Huthwelker, F. d'Acapito, G. Schumacher, *Acta Materialia* **2020**, *193*, 329-337.
37 Z. Sun, C. Hao, S. Toan, R. Zhang, H. Li, Y. Wu, H. Liu, Z. Sun, *Journal of Materials Chemistry A* **2023**, *11*, 17961-17976.
38 S. Albonetti, A. Lolli, V. Morandi, A. Migliori, C. Lucarelli, F. Cavani, *Applied Catalysis B: Environmental* **2015**, *163*, 520-530.
39 C. Gai, F. Zhang, T. Yang, Z. Liu, W. Jiao, N. Peng, T. Liu, Q. Lang, Y. Xia, *Green chemistry* **2018**, *20*, 2788-2800.
40 B. Zhao, P. Liu, S. Li, *Applied Catalysis B: Environmental* **2020**, *278*, 119307.
41 R. Matsumoto, S. Seki, S. Taketomi, N. Miyazaki, *Computational Materials Science* **2014**, *92*, 362-371.
42 Q. Ji, L. Bi, J. Zhang, H. Cao, X. S. Zhao, *Energy & Environmental Science* **2020**, *13*, 1408-1428.
43 H. Idriss, *Surface science* **2021**, *712*, 121894.
44 O. Kwon, S. Sengodan, K. Kim, G. Kim, H. Y. Jeong, J. Shin, Y.-W. Ju, J. W. Han, G. Kim, *Nature communications* **2017**, *8*, 15967.
45 Y. Han, J. Xu, W. Xie, Z. Wang, P. Hu, *ACS catalysis*, **2023**, *13(22)*, 15074-15086.
46 B. Lu, T. Zhang, L. Zhang, Y. Xu, Z. Zhang, F. Wu, X. Li, C. Luo, *Applied Surface Science*, **2022**, *587*, 152881.
47 Y. Yu, G. Jin, Y. Wang, XY. Guo, *Catalysis Communications*, **2013**, *31*, 5-10.
48 C .Wang, W. Liu, M. Liao, J. Weng, J. Shen, Y. Chen, Y. Du. *Nanoscale*, **2023**, *15(19)*, 8619-8632.
49 Z. Ou, J. Ran, J. Niu, Z. Zhang, T. Deng, Z. He, C. Qin, *International Journal of Hydrogen Energy* **2020**, *45*, 31849-31862.
50 E. T. Saw, U. Oemar, X. Tan, Y. Du, A. Borgna, K. Hidajat, S. Kawi, *Journal of catalysis* **2014**, *314*, 32-46.
51 M. Andersson, F. Abild-Pedersen, I. Remediakis, T. Bligaard, G. Jones, J. Engbæk, O. Lytken, S. Horch, J. H. Nielsen, J. Sehested, *Journal of Catalysis* **2008**, *255*, 6-19.
52 S. Godoy, P. Deshlahra, F. Villagra-Soza, A. Karelovic, R. Jimenez, *Catalysts* **2022**, *12*, 1380.
53 F. Lu, L. Wen, Y. Zhao, H. Zhong, J. Xu, S. Zhang, Z. Yang, *International Journal of Hydrogen Energy* **2019**, *44*, 6427-6436.

54 Z. Jia, N. Ji, X. Diao, X. Li, Y. Zhao, X. Lu, Q. Liu, C. Liu, G. Chen, L. Ma, *ACS Catalysis* **2022**, *12*, 1338-1356.

55 X. Sheng Li, W. Zhao Li, Y. Xin Chen, H. L. Wang, *Catalysis letters* **1995**, *32*, 31-42.